Membrane filtration with multiple fouling mechanisms

Pejman Sanaei ◉[*]

Department of Mathematics, New York Institute of Technology, New York, New York 10023-7692, USA

Linda J. Cummings

Department of Mathematical Sciences and Center for Applied Mathematics and Statistics,
New Jersey Institute of Technology, Newark, New Jersey 07102-1982, USA

Manufacturers of membrane filters have an interest in optimizing the internal pore structure of the membrane to achieve the most efficient filtration. As filtration occurs, the membrane becomes fouled by impurities in the feed solution, and any effective model of filter performance must account for this. In this paper, we present a simplified mathematical model, which (i) characterizes membrane internal pore structure via permeability or resistance gradients in the depth of the membrane; (ii) accounts for multiple membrane fouling mechanisms (adsorption, blocking, and cake formation); (iii) defines a measure of filter performance; and (iv) for given operating conditions, is able to predict the optimum permeability or resistance profile for the chosen performance measure.

I. INTRODUCTION

Membrane filters—thin sheets of porous medium that act to separate contaminants from a fluid—find widespread use for applications as diverse as water treatment [1], purification processes in the biotech industry [2–5], kidney dialysis [6], and beer clarification [7,8]. Major multinational companies such as W.L. Gore & Associates, Pall Corporation, EMD Millipore, and GE Healthcare Life Sciences manufacture a wide range of membrane-based filtration products and maintain a strong interest in improving and optimizing the filters they produce, in terms of both performance and cost. Filter membrane performance (discussed in more detail later) is affected by a number of key design features, such as the membrane thickness, internal pore structure and shape, pore connectivity, variation of pore dimensions in the depth of the membrane, and membrane material. As a filtration progresses, the particles removed from the feed solution are deposited on or in the membrane, and understanding and prediction of the flow and fouling in the filter membrane is a critical part of the design process. Experimental approaches are costly and it is difficult to visualize accurately where particles are trapped in the depth of the membrane. Mathematical modeling can therefore help manufacturers gain insight into filtration processes and operating conditions and thus provide a cost-effective way to help optimize filter design [9–11].

Various modeling approaches, which attempt to determine how the internal structure of filter membranes (pores' size, geometry, and distribution within the membrane) influences filtration efficiency, have been proposed and examined by researchers to date. Among these, computational fluid dynamics (CFD) is popular and effective, offering the capability to track the fate of all particles within the feed, and to predict internal blocking well. Proprietary CFD software is used

---

[*]psanaei@nyit.edu

(in conjunction with sophisticated 3D imaging that can provide detailed pore structure) by several industries to help simulate and evaluate membrane performance [12]. Such CFD simulations are very expensive computationally [13] and are limited to fairly small membrane samples and moderate times; nevertheless they still represent a cheaper means (in terms of both time and actual expense) to probe the effects of membrane structural changes than do experiments. The high computational cost stems mainly from the complicated membrane internal morphology, which forms the computational domain of the governing fluid dynamics equations. An interesting review of the scope of CFD modeling in membrane separation was compiled by Ghidossi *et al.* in 2006 [14]; see also Refs. [15–17] for a discussion of more recent contributions in this area (among other topics).

To avoid the high computational costs associated with the CFD approach (allowing for larger membrane domains to be simulated, for longer periods of time) and to gain greater mechanistic insight into the fouling, others have used different modeling techniques. In much of the filtration literature four distinct fouling modes are identified: (a) standard blocking, also known as adsorptive fouling (in which particles smaller than the membrane pores are deposited or adsorbed within pores, shrinking the pore diameter); (b) intermediate blocking (the partial blocking of a pore by a large particle at its upstream opening); (c) complete blocking (the total blocking of a pore by a large particle at its upstream opening); and (d) cake formation (once pores are blocked by large particles, other particles can accumulate on top of the membrane, forming a "cake" layer). All of these fouling modes add resistance to the system. Various (non-CFD) mechanistic filtration models that account for one or more of these fouling modes, and/or allow depth-dependent membrane structure (permeability gradients) to be modeled, have been proposed to date. The literature is vast and we do not attempt a comprehensive overview here, mentioning just a few of the approaches most relevant to our work, and referring the interested reader to dedicated review articles (e.g., Refs. [1,18] and and references therein).

Homogenization methods have been considered by several authors [19–26]. Homogenization alleviates the complexity of the problem by averaging micro-scale properties of the feed solution (called "solvent" in the language of homogenization theory) or membrane over mesoscale units that repeat periodically (or nearly so) across the macroscale domain. Recent notable work in this area was carried out by Dalwadi *et al.* [21] and Griffiths *et al.* [22]. Dalwadi *et al.* [21] use their model to explore how filtration efficiency can be improved when the (continuously varying) porosity gradient is appropriately tuned. The results show qualitative agreement with experimental observations; however the model considers only a single fouling mechanism: the "standard blocking" or adsorptive fouling, described above. Griffiths *et al.* [22] demonstrate the efficiency of a multilayer filter based on a so-called network model, developed earlier by the same group [9]. This work accounts for two fouling mechanisms: the adsorptive fouling, plus blocking by large particles. However, the model fails to account for fouling by cake formation.

In models that account for cake formation, some studies, e.g., Refs. [2,27–29] allow pore blocking and cake formation to happen simultaneously during the fouling process, but more commonly pore blocking is assumed to precede cake formation. Bolton *et al.* [2] derived models that accounted for the combined simultaneous effects of any two individual fouling mechanisms (standard, intermediate/complete blocking; and cake formation). These authors used Darcy's law to relate the instantaneous pressure drop to time for a filter operating under conditions of constant flux; and to throughput (cumulative volume filtered) under conditions of constant pressure. The combined models were assessed through testing with solutions of bovine serum albumin and human IgG, filtered through virus retention and sterilizing grade microporous membranes, respectively. All models were found to be useful within certain parameter regimes (within which at least one fouling mechanism is negligible), providing good fits of the presented data sets.

Contemporaneously, Duclos-Orsello *et al.* [30] also developed a multimode fouling model, sequentially accounting for adsorptive fouling, complete blocking and cake formation. In this study, initially, pore constriction occurs in all open pores; then undergo blocking, to form an inhomogeneous surface on which the cake layer finally forms. Once a pore is blocked by a deposited

aggregate, no further pore constriction can occur. This work, as with that of Bolton *et al.* [2], is based on the assumption of circularly-cylindrical pores that traverse the membrane depth. The model was tested on a range of datasets, both with and without prefiltration of the feed, and was found capable of simulating all, with suitable parameter choices. This is the key advantage of such a universal fouling model: the same model can be used to simulate almost any filtration for its entire duration, whether it is a prefiltration stage in which complete blocking and cake formation dominate; ultrafiltration of a feed suspension with only very fine particles in which adsorptive fouling dominates; or a low-tech simplistic filtration in which all mechanisms may be fully operational. The model user just has to make appropriate parameter choices to ensure that the relevant mechanisms dominate (or can even turn off one or more mechanisms altogether if desired). In this respect, however, the authors note while discussing one dataset that even "while the slope...indicates that fouling is dominated by pore constriction, we see from the values of the other [fitted] parameters that fouling is actually caused by all three fouling mechanisms." Similar remarks are noted for another dataset. Thus, it is suggested that more accurate simulations will be obtained using a multi-mode fouling model, and that indeed such models can provide greater insight into when different fouling modes may be expected to be important, and at what stage of a filtration transitions between different fouling modes are expected.

In earlier work [10], we developed a model that can describe the key effects of membrane morphology on separation efficiency and fouling of a membrane filter. That model accounts for Darcy flow through the membrane, and for two distinct mechanisms of fouling: adsorption of small particles within pores, and pore-blocking (sieving) by large particles. In the present paper, we propose a model for the formation and growth of a cake layer on the upstream side of the filter, and couple this to our earlier model, to allow all three fouling modes (rather than just two mechanisms as considered in Ref. [2]) to operate simultaneously. Such a "unified" model, properly validated and calibrated, can be used to describe a very wide range of filtration scenarios, including those where only one or two of the mechanisms may be relevant at any given stage of the filtration. This represents an important extension to the work of Duclos-Orsello *et al.* [30] in that our model allows for depth-dependent pore structure (porosity gradients), known to be important in many applications.

We present several simulations of our model, with an emphasis on how the fouling by cake formation affects results, and how changes in membrane structure (modeled by different choices of pore profile within the membrane) may impact the outcome (most multimode fouling models, such as Refs. [2,30], consider only membranes with cylindrical pores). In particular, we discuss how our model could be used to provide guidance as to the optimum porosity gradient that a membrane filter should have. We conclude with a discussion of our model and results in the context of real membrane filters. Note that the results of this paper as presented are intended to be illustrative of the model's capability to provide useful information and predictions, given reliable parameter estimates. We do not suggest that the pore structures calculated for our sample simulations will be optimal in all scenarios. However, our model could be used to carry out optimization for a given application, once specific model parameters relevant to that application have been determined via experiments.

II. DARCY FLOW AND FOULING MODEL

We consider dead-end filtration through a planar membrane that lies parallel to the (Y, Z) plane, with unidirectional Darcy flow through the membrane in the positive X direction. The membrane properties and flow are assumed homogeneous in the (Y, Z) plane, but the membrane has depth-dependent permeability (even if permeability is initially uniform in X, fouling will lead to nonuniformities over time), which we denote by $K_m(X, T)$. We use uppercase fonts to denote dimensional quantities, and in the following will introduce subscripts "m" and "c" to distinguish (where necessary) between quantities in the membrane and in the cake layer.
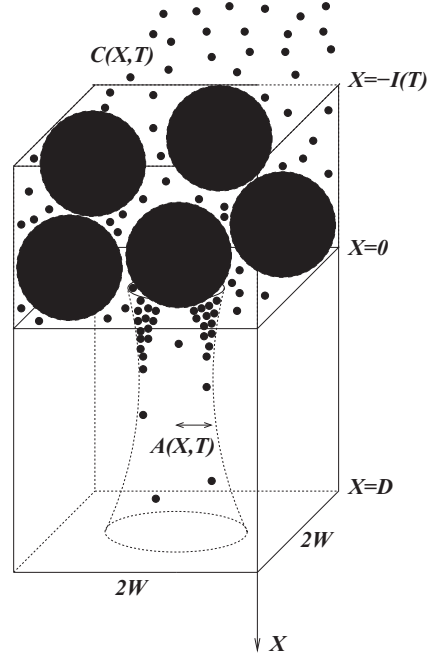
FIG. 1. Schematic showing the pore, the small particles leading to adsorptive fouling, and the forming cake layer consisting of large particles. Here, $C(X, T)$ denotes the concentration of the small particles, while $A(X, T)$ denotes the radius of the pore, at depth X and time T.

The superficial Darcy velocity $\mathbf{U} = [U(X, T), 0, 0]$ within the membrane is given in terms of the pressure P_{m} by

$$U = -\frac{K_{\mathrm{m}}(X, T)}{\mu} \frac{\partial P_{\mathrm{m}}}{\partial X}, \quad \frac{\partial U}{\partial X} = 0, \quad 0 \leqslant X \leqslant D, \tag{1}$$

where μ is the viscosity of the feed solution (assumed Newtonian) and D is the membrane thickness.[1] The membrane permeability $K_{\mathrm{m}}(X, T)$ is a function of membrane characteristics, which evolve in time due to fouling. We allow K_{m} to decrease in time (i.e., membrane resistance increases in time) via three fouling mechanisms: (i) pores become blocked from above by particles too large to pass through pores; (ii) pore radius decreases in time due to adsorption of smaller particles within the pores; and (iii) at a late stage, particles deposited on the filter upstream form a cake layer. This cake layer is assumed to occupy the region $-I(T) \leqslant X \leqslant 0$, so that $I(T)$ is the cake thickness, with $I(0) = 0$.

We consider a simple model in which the membrane consists of a series of identical axisymmetric slender pores of variable radius $A(X, T)$, which traverse the membrane thickness (Fig. 1). Pores are arranged in a square repeating lattice, with period $2W$, and a feed solution, carrying *small* particles [at concentration $C(X, T)$] and *large* particles (larger than pores; with concentration G in the feed), which are deposited within the membrane and on top of the membrane, respectively, is driven through the filter. In many applications there will in fact be a continuum of particle sizes: our model

---

[1]Note that the Darcy velocity U does not require a subscript to distinguish between membrane and cake layers since it is independent of X.

is an idealization in which all particles larger than pores are modeled as a single population leading to fouling by complete blocking and later cake formation; while all particles smaller than pores are treated as a separate population giving rise to adsorptive fouling. Two driving mechanisms are commonly considered: (i) constant pressure drop across the membrane specified; and (ii) constant flux through the membrane specified. In the former case, the flux decreases in time as the membrane becomes fouled; in the latter case, the pressure drop required to sustain the constant flux rises as fouling occurs. In this paper we consider only case (i), which is the most common in practice [our model could be easily adapted to case (ii)]. With constant pressure drop P_0, the conditions applied above and below the membrane plus cake are

$$P_c(-I(T), T) = P_0, \quad P_m(D, T) = 0, \tag{2}$$

where P_c is the pressure within the cake, and $X = -I(T)$ is the top of the cake (see Fig. 1). The flow through the cake layer is described in Sec. II C below.

Where an individual pore (at time T) is unblocked the total flux through it $Q_{u,pore}(T)$ is given, approximately, by

$$Q_{u,pore} = -\frac{1}{R_u}\frac{\partial P_m}{\partial X}, \quad \text{where} \quad R_u = \frac{8\mu}{\pi A^4}, \tag{3}$$

and R_u is the local pore resistance per unit of the membrane depth.

A. Pore blocking by large particles

Blocking occurs when a particle from our population of large particles becomes trapped at the entrance to a pore, obstructing the flow. We follow our earlier approach [10,31] and model this effect by adding an extra resistance, of magnitude $8\mu\rho_b/(\pi A_0^4)$ (per unit of the membrane depth), in series with the resistance R_u. Here ρ_b is a dimensionless number representing the factor by which the pore's resistance is increased on blocking (relative to the unblocked state). The flux through a blocked pore, $Q_{b,pore}(X, T)$, is then given by

$$Q_{b,pore} = -\frac{1}{R_b}\frac{\partial P_m}{\partial X} \quad \text{where} \quad R_b = \frac{8\mu}{\pi A_0^4}\left[\left(\frac{A_0}{A}\right)^4 + \rho_b\right]. \tag{4}$$

The parameter ρ_b characterizes the tightness of the seal formed by a blocking event: for large values of ρ_b the seal is tight and pore resistance increases dramatically after blocking, while for small values the seal is very weak, and resistance is almost unchanged. A perfectly sealed pore (total blocking) is retrieved as $\rho_b \to \infty$. We can now relate the superficial Darcy velocity U to the number densities of unblocked and blocked pores per unit area, $N(T)$ and $N_0 - N(T)$, respectively (where $N_0 = N(0)$ and $N_0(2W)^2 = 1$), by noting that the flux of fluid per unit area of membrane is

$$N_0(2W)^2 U = N(T)Q_{u,pore} + (N_0 - N(T))Q_{b,pore},$$

hence, substituting for $Q_{u,pore}$ from Eq. (3) and for $Q_{b,pore}$ from Eq. (4) in the above, we obtain

$$U = -\frac{\pi A_0^4}{8\mu}\frac{\partial P_m}{\partial X}\left[\frac{N}{(A_0/A)^4} + \frac{N_0 - N}{(A_0/A)^4 + \rho_b}\right]. \tag{5}$$

The instantaneous number density of unblocked pores, $N(T)$, decreases as pores become blocked. We assume blockage occurs whenever a particle with radius $S > A(X, T)$ is advected to the pore entrance. For simplicity, we assume that our large-particle population consists entirely of particles larger than $A(0, T)$, while our small-particle population (discussed below) consists of particles that are smaller than $A(X, T)$ throughout. It would not be difficult to modify our model to allow for blocking events in the pore interior; however, the resulting model would be more cumbersome and would not, we believe, lead to substantially different predictions. If G is the concentration of

large particles in the feed, then the probability, per unit time, that a particular pore is blocked, is $GQ_{\mathrm{u,pore}} = -\pi G A^4/(8\mu)\partial P_{\mathrm{m}}/\partial X|_{X=0}$. It follows that $N(T)$ evolves according to

$$\frac{\partial N}{\partial T} = NG\frac{\pi A^4}{8\mu}\frac{\partial P_{\mathrm{m}}}{\partial X}\bigg|_{X=0}. \tag{6}$$

B. Pore blocking by adsorption

To model adsorptive fouling requires consideration of how the small particles in the feed are transported and deposited within the pores of the membrane. Following Ref. [10], we propose a simple advection model for the concentration of small particles, C_{m}, within the membrane pores, which posits that particles are deposited on the pore wall at a rate proportional to both the local particle concentration, and to the inverse of the local pore radius:

$$U_{\mathrm{pm}}\frac{\partial C_{\mathrm{m}}}{\partial X} = -\Lambda_{\mathrm{m}}\frac{C_{\mathrm{m}}}{A}, \quad 0 \leqslant X \leqslant D, \tag{7}$$

where U_{pm} is the pore velocity of the feed within the membrane (the cross-sectionally averaged axial velocity within each membrane pore) and Λ_{m} is a constant that models the attraction between particles and pore wall that is causing the deposition. A full derivation of this model, which arises from a particular limit in which particle diffusion dominates in the pore cross-section but advection dominates in the axial direction, is given in Ref. [10]. The pore velocity U_{pm} satisfies

$$\frac{\partial(\pi A^2 U_{\mathrm{pm}})}{\partial X} = 0, \quad 4W^2 U = \pi A^2 U_{\mathrm{pm}}, \tag{8}$$

by simple mass conservation arguments. The pore radius shrinks in response to the particle deposition; we propose

$$\frac{\partial A}{\partial T} = -\Lambda_{\mathrm{m}}\alpha C_{\mathrm{m}}, \quad 0 \leqslant X \leqslant D, \tag{9}$$

for some constant α (proportional to the particle size). The initial pore radius is specified throughout the membrane,

$$A(X, 0) = A_0(X), \quad 0 \leqslant X \leqslant D. \tag{10}$$

C. Cake formation

In the later stages of filtration, subsequent to the pore-blocking described in Sec. II A above, particles may accumulate on the upstream side of the membrane, forming a *cake* layer as shown in Fig. 1. This layer in turn increases the system resistance and becomes thicker in time. To obtain realistic predictions throughout the entire filtration process, particularly for cases where the feed contains a high concentration of large particles, we must consider the effects of the cake layer.

To model caking, we assume that pore-blocking by large particles at the upstream membrane surface creates new surface area available for formation of a cake layer. If we assume that material (comprising large particles) is deposited on this available surface at a rate proportional to the fluid flux and to the number of blocked pores (which constitute the available surface), then we may propose a model for how the cake layer thickness $I(T)$ increases in time:

$$\frac{dI}{dT} = (N_0 - N)(2W)^2(G\Delta_{\mathrm{p}})U, \quad I(0) = 0, \tag{11}$$

where G is the total large-particle concentration defined earlier, U is the superficial Darcy velocity [defined in Eq. (5)], and Δ_{p} is the effective volume that each large particle occupies within the cake layer. This model says that the thickness of cake layer increases at a rate proportional to the membrane area available for caking, and the volume flux of the large particles that form the cake.

At the cake's upper surface we specify the pressure, Eq. (2), and the small-particle concentration,

$$C_c(-I(T), T) = C_0. \tag{12}$$

The cake layer itself behaves like a secondary filter membrane, with permeability $K_c(X, T)$ dependent on the characteristics of the particles suspended in the feed solution. We therefore again use the Darcy model to describe flow across the cake:

$$U = -\frac{K_c}{\mu}\frac{\partial P_c}{\partial X}, \quad -I(T) \leqslant X \leqslant 0, \quad P_c(-I(T), T) = P_0. \tag{13}$$

Though the cake is assumed to be composed primarily of the large particles, like the membrane it will be subject to adsorptive fouling by smaller particles, which will deposit in the gaps between the large particles. Its permeability, K_c, will thus decrease in time. We use the Kozeny-Carman equation (see, e.g., Ref. [32]) to relate K_c to the void fraction (or porosity), $\phi_c \in (0, 1)$, of the cake:

$$K_c = \frac{\phi_c^3}{K_{oz}S_{cp}^2(1 - \phi_c)^2}. \tag{14}$$

Here, S_{cp} is the specific area (the ratio of the surface area to the volume of the solid fraction of the porous medium); and K_{oz} is the Kozeny constant (Carman proposed a value of 5 for this constant; see, e.g., Ref. [32]). Note that due to the adsorption of the smaller particles within the cake, ϕ_c will decrease monotonically in T and also develop depth dependence, $\phi_c(X, T)$. If at early times the cake layer is considered to consist of identical randomly packed spherical particles, then we might expect $\phi_c \approx 0.37$, with this value decreasing as adsorption occurs. The cake model is completed by assumptions about how adsorption leads to increased cake resistance. In the spirit of our membrane fouling model Eq. (7) we propose a simple advection model for the small particles:

$$U_{pc}\frac{\partial C_c}{\partial X} = -\Lambda_c\frac{C_c}{(\phi_c\Delta_p)^{1/3}}, \quad -I(T) \leqslant X \leqslant 0, \tag{15}$$

where the pore velocity U_{pc} within the cake is related to the superficial Darcy velocity U by $U_{pc} = U/\phi_c$. As with the membrane, we assume that small particles are deposited within the cake at a rate proportional to their local concentration. The constant Λ_c models the attraction between the large particles (which constitute the cake) and the small particles. The cake structure is complicated, but in essence the pores of the cake consist of the spaces between particles of effective volume Δ_p, therefore we assume that $(\phi_c\Delta_p)^{1/3}$ will be proportional to the cake pore size [whence the term in the denominator on the right-hand side of Eq. (15); compare with Eq. (7)]. The cake porosity ϕ_c decreases in response to the particle deposition: By direct analogy with our earlier membrane adsorptive fouling model [see Eq. (9) with pore size $A \propto (\phi_c\Delta_p)^{1/3}$], we propose

$$\frac{\partial \phi_c}{\partial T} = -\Lambda_c(\phi_c\Delta_p)^{2/3}C_c, \quad -I(T) \leqslant X \leqslant 0. \tag{16}$$

Equations (15) and (16) are analogous to Eqs. (7) and (9) in the membrane model, respectively. We also require continuity of particle concentration and pressure at the interface between the cake layer and the membrane,

$$C_c(0, T) = C_m(0, T), \quad P_c(0, T) = P_m(0, T). \tag{17}$$

For future reference, we note the simple pressure drop equation,

$$\triangle P|_{-I(T)}^D = \triangle P_m|_0^D + \triangle P_c|_{-I(T)}^0, \tag{18}$$

or, in integral form,

$$\int_{-I(T)}^D \frac{\partial P}{\partial X}dX = \int_0^D \frac{\partial P_m}{\partial X}dX + \int_{-I(T)}^0 \frac{\partial P_c}{\partial X}dX. \tag{19}$$

III. SCALING AND NONDIMENSIONALIZATION

We nondimensionalize the model presented above using the scalings

$$(X, I) = D(x, i), \quad A = Wa, \quad T = \frac{8\mu D}{\pi P_0 W^4 G} t, \quad (U, U_{\mathrm{pm}}, U_{\mathrm{pc}}) = \frac{\pi P_0 W^2}{32\mu D}(u, u_{\mathrm{pm}}, u_{\mathrm{pc}}),$$

$$(P_{\mathrm{m}}, P_{\mathrm{c}}) = P_0(p_{\mathrm{m}}, p_{\mathrm{c}}), \quad (C_{\mathrm{m}}, C_{\mathrm{c}}) = C_0(c_{\mathrm{m}}, c_{\mathrm{c}}), \quad N = N_0 n, \quad K_{\mathrm{c}} = \frac{\pi W^2}{32} k_{\mathrm{c}}, \tag{20}$$

giving a dimensionless model for $u(x, t)$, $u_{\mathrm{pm}}(x, t)$, $u_{\mathrm{pc}}(x, t)$, $p_{\mathrm{m}}(x, t)$, $p_{\mathrm{c}}(x, t)$, $a(x, t)$, $c_{\mathrm{m}}(x, t)$, $c_{\mathrm{c}}(x, t)$, $i(t)$, $k_{\mathrm{c}}(t)$, $\phi_{\mathrm{c}}(t)$, and $n(t)$. The dimensionless governing equations in the membrane layer $0 \leqslant x \leqslant 1$ become

$$4u = \pi a^2 u_{\mathrm{pm}}, \tag{21}$$

$$u = -a^4 \frac{\partial p_{\mathrm{m}}}{\partial x}\left(\frac{1-n}{1+\rho_{\mathrm{b}} a^4} + n\right), \quad \frac{\partial u}{\partial x} = 0, \tag{22}$$

$$u_{\mathrm{pm}}\frac{\partial c_{\mathrm{m}}}{\partial x} = -\lambda_{\mathrm{m}}\frac{c_{\mathrm{m}}}{a}, \quad \lambda_{\mathrm{m}} = \frac{32\Lambda_{\mathrm{m}}\mu D^2}{\pi P_0 W^3}, \tag{23}$$

$$\frac{\partial a}{\partial t} = -\beta_{\mathrm{m}} c_{\mathrm{m}}, \quad \beta_{\mathrm{m}} = \frac{8\mu D\Lambda_{\mathrm{m}}\alpha C_0}{\pi P_0 W^5 G}, \tag{24}$$

$$\frac{dn}{dt} = na^4 \frac{\partial p_{\mathrm{m}}}{\partial x}\bigg|_{x=0}, \tag{25}$$

with boundary and initial conditions

$$p_{\mathrm{m}}(1, t) = 0, \quad a(x, 0) = a_0(x), \tag{26}$$

where $a_0(x) < 1$ is a specified function.

The governing equations in the cake layer $-i(t) \leqslant x \leqslant 0$ are:[2]

$$u_{\mathrm{pc}} = \frac{u}{\phi_{\mathrm{c}}}, \tag{27}$$

$$u = -k_{\mathrm{c}}\frac{\partial p_{\mathrm{c}}}{\partial x}, \quad \frac{\partial u}{\partial x} = 0, \tag{28}$$

$$k_{\mathrm{c}} = \kappa_{\mathrm{c}}\frac{\phi_{\mathrm{c}}^3}{(1-\phi_{\mathrm{c}})^2}, \quad \kappa_{\mathrm{c}} = \frac{32}{\pi W^2 K_{\mathrm{oz}} S_{\mathrm{cp}}^2}, \tag{29}$$

$$\frac{\partial \phi_{\mathrm{c}}}{\partial t} = -\beta_{\mathrm{c}} c_{\mathrm{c}}\phi_{\mathrm{c}}^{2/3}, \quad \beta_{\mathrm{c}} = \frac{8\mu D\Lambda_{\mathrm{c}}\Delta_{\mathrm{p}}^{2/3} C_0}{\pi P_0 W^4 G}, \tag{30}$$

$$u_{\mathrm{pc}}\frac{\partial c_{\mathrm{c}}}{\partial x} = -\lambda_{\mathrm{c}}\frac{c_{\mathrm{c}}}{\phi_{\mathrm{c}}^{1/3}}, \quad \lambda_{\mathrm{c}} = \frac{32\Lambda_{\mathrm{c}}\mu D^2}{\pi P_0 W^2 \Delta_{\mathrm{p}}^{1/3}}, \tag{31}$$

$$\frac{di}{dt} = \eta(1-n)u, \quad \eta = \frac{\Delta_{\mathrm{p}}}{4W^2 D}, \tag{32}$$

with boundary and initial conditions

$$p_{\mathrm{c}}(-i(t), t) = 1, \quad c_{\mathrm{c}}(-i(t), t) = 1. \tag{33}$$

---

[2]The cake model presented implicitly assumes that the specific area, S_{cp}, is constant throughout. This will not quite be true, but we believe it is reasonable to neglect its evolution due to fouling.

The model is closed by continuity conditions at the membrane–cake interface,

$$c_c(0, t) = c_m(0, t), \quad p_c(0, t) = p_m(0, t), \tag{34}$$

and by the flux balance equations

$$4\phi_c u_{pc} = 4u = \pi a^2 u_{pm}. \tag{35}$$

Significant analytical progress may be made with this model. Equations (22) with the boundary condition at the pore outlet, $p_m(1, t) = 0$, give the pressure within the membrane, $p_m(x, t)$, as

$$p_m(x, t) = u \int_x^1 \frac{dx'}{a^4 \left(\frac{1-n}{1+\rho_b a^4} + n \right)}, \tag{36}$$

while Eqs. (28) and (33) give the pressure in the cake layer as

$$p_c(x, t) = 1 - u \int_{-i(t)}^x \frac{dx'}{k_c}. \tag{37}$$

By using the continuity condition Eq. (34) for the pressure, we find the dimensionless Darcy velocity as

$$u = \left(\int_{-i(t)}^0 \frac{dx'}{k_c} + \int_0^1 \frac{dx'}{a^4 \left(\frac{1-n}{1+\rho_b a^4} + n \right)} \right)^{-1}. \tag{38}$$

From Eq. (25) the number of unblocked pores satisfies

$$\frac{dn}{dt} = -n \left(\int_{-i(t)}^0 \frac{dx'}{k_c} + \int_0^1 \frac{dx'}{a^4 \left(\frac{1-n}{1+\rho_b a^4} + n \right)} \right)^{-1} \left(\frac{1-n}{1+\rho_b a^4} + n \right)^{-1} \Bigg|_{x=0}, \tag{39}$$

and the cake layer thickness can be easily found from Eq. (32),

$$\frac{di}{dt} = \eta(1-n) \left(\int_{-i(t)}^0 \frac{dx'}{k_c} + \int_0^1 \frac{dx'}{a^4 \left(\frac{1-n}{1+\rho_b a^4} + n \right)} \right)^{-1}. \tag{40}$$

Finally, we simplify Eqs. (23) and (31) for particle concentration within the membrane and the cake layer as

$$\frac{\partial c_m}{\partial x} = -\lambda_m c_m a \left(\int_{-i(t)}^0 \frac{dx'}{k_c} + \int_0^1 \frac{dx'}{a^4 \left(\frac{1-n}{1+\rho_b a^4} + n \right)} \right), \quad c_m(0, t) = c_c(0, t), \quad \lambda_m = \frac{8\Lambda_m \mu D^2}{P_0 W^3}, \tag{41}$$

$$\frac{\partial c_c}{\partial x} = -\lambda_c \phi_c^{2/3} c_c \left(\int_{-i(t)}^0 \frac{dx'}{k_c} + \int_0^1 \frac{dx'}{a^4 \left(\frac{1-n}{1+\rho_b a^4} + n \right)} \right), \quad c_c(-i(t), t) = 1, \tag{42}$$

and we have the pore shrinkage equation

$$\frac{\partial a}{\partial t} = -\beta_m c_m, \tag{43}$$

where β_m is given in Eq. (24).

IV. RESULTS

In this section we present sample simulations of the model summarized in Sec. III, highlighting how results depend on the key parameters governing the cake formation. Our model contains several

TABLE I. Dimensional parameters and approximate values (Refs. [33,34]).

Parameter	Description	Typical Value
P_0	Pressure drop	Depends on application (10–100 K Pa used here)
Q_{pore}	Flux through a single pore	Depends on application
C_0	Total concentration of small particles in feed	Depends on application
G	Total concentration of large particles in feed	Depends on application
$2W$	Length of the square repeating lattice	4.5 μm (very variable)
D	Membrane thickness	30 μm (very variable)
A_0	Initial pore radius	2 μm (very variable)
N_0	Number of pores per unit area	7×10^{10} m^{-2} (very variable)
Λ_{m}	Particle-wall attraction coefficient	Unknown (depends on details of membrane and feed solution)
Λ_{c}	Small particle-large particle attraction coefficient	Unknown (depends on feed solution)
α	Pore shrinkage parameter [see Eq. (9)] proportional to particle size	Depends on application
Δ_{p}	Effective particle volume within the cake layer	4×10^{-16} m^3 (very variable)
K_{oz}	Kozeny constant	5
S_{cp}	Specific area; the ratio of surface area to the volume of the solid fraction in the cake	1.35 μm^{-1} (very variable)

dimensionless parameters and functional inputs, which must be specified: λ_{m}, which measures the attraction between the small particles and the membrane pore wall (characterizing the strength of adsorptive fouling); λ_{c}, which measures the attraction between small particles and the large particles that form the cake layer (governing adsorption of small particles within the cake itself); β_{m}, the dimensionless membrane pore shrinkage rate; β_{c}, the rate at which porosity of the cake layer decreases; ρ_{b}, the factor by which pore-blocking by a large particle increases the original resistance of the unblocked pore; κ_{c}, the characteristic dimensionless cake permeability; and η, the dimensionless characteristic rate at which cake layer thickness increases. An exhaustive investigation of the effects of all parameters is clearly impractical. Their values depend on physical dimensional parameters that must be measured for the particular system under investigation, and in many cases reliable data are lacking, hence we have to make our best guess as to the most appropriate values to use in simulations. The parameters are summarized in Tables I (dimensional parameters) and II (dimensionless parameters) along with typical values, where known. Although a high level of variability or uncertainty in parameter values is noted, in practice users and filter membrane manufacturers should together be able to provide values or estimates for most of the parameters listed in Table I for specific applications (such as P_0, Q_{pore}, C_0, G, W, D, A_0, N_0, α, Δ_{p}, and S_{cp}), which depend on physical characteristics of the filter membrane and the feed fluid. Certain other parameters, for example the particle-wall and the small particle-large particle attraction coefficients Λ_{m} and Λ_{c}, respectively, are more difficult to estimate and will require preliminary experiments. Methods such as fluorescence microscopy (see Jackson *et al.* [35]), with particles in the feed suspension fluorescently tagged, can be used to estimate Λ_{m} and Λ_{c} by comparing solutions of Eqs. (9) and (16) to experimental images that reveal the density and location of particles trapped within the filter and in the cake layer.

Given the number of parameters, many will be held fixed throughout our simulations. The values of the dimensionless attraction coefficients between pore wall and particles, and between large and small particles in the cake layer, λ_{m} and λ_{c}, respectively, are unknown, and could vary considerably from one system to another. In the absence of definitive data, we take $\lambda_{\mathrm{m}} = 2$ and $\lambda_{\mathrm{c}} = 0.5$ as the default values (since the filter is designed to remove particles, we assume that the particles are more strongly attracted to the membrane than to the cake, hence $\lambda_{\mathrm{m}} > \lambda_{\mathrm{c}}$). The dimensionless membrane

TABLE II. Dimensionless parameter definitions and values used.

Parameter	Formula and description	Typical value
λ_{m}	$(8\Lambda_{\mathrm{m}}\mu D^2)/(P_0 W^3)$ Dimensionless particle-pore wall attraction coefficient	Unknown; value 2 used
λ_{c}	$(32\Lambda_{\mathrm{c}}\mu D^2)/(\pi P_0 W^2 \Delta_{\mathrm{p}}^{1/3})$ Dimensionless attraction coefficient between small particles and cake	Unknown; values in range 0.1–5 used
$\bar{\phi}_{\mathrm{m}}$	$\pi/(4W^2)\int_0^D A^2 dX$ Net (initial) membrane porosity or void fraction	Varies in range 0.5–0.7
β_{m}	$(8\mu D\Lambda_{\mathrm{m}}\alpha C_0)/(\pi P_0 W^5 G)$ Membrane pore shrinkage rate due to adsorption	Unknown; values in range 0.1–0.2 used
β_{c}	$(8\mu D\Lambda_{\mathrm{c}}\Delta_{\mathrm{p}}^{2/3} C_0)/(\pi P_0 W^4 G)$ Cake pore shrinkage rate due to adsorption	Unknown; values in range 0.1–1 used
ρ_{b}	Additional constant resistance when pore becomes blocked by a large particle	Unknown; value 2 used
η	$\Delta_{\mathrm{p}}/(4W^2 D)$ Cake layer thickness growth rate	Unknown; values in range 0.1–2 used
κ_{c}	$32/(\pi W^2 K_{\mathrm{oz}} S_{\mathrm{cp}}^2)$ Cake permeability coefficient	Unknown; value 1 used

and cake pore shrinkage rates, β_{m} and β_{c}, respectively, are not known precisely, and indeed depend strongly on the characteristics of the feed solution (these represent the ratios of the timescales of adsorptive pore closure, in membrane and cake, respectively, to pore blocking). Since in this paper we are primarily interested in filtration regimes where cake formation plays a significant role, we take rather small values for these coefficients: We set the default values to $\beta_{\mathrm{m}} = \beta_{\mathrm{c}} = 0.1$ [in particular, $O(1)$ or larger values for β_{m} would give adsorption-dominated fouling, which has been studied elsewhere]. Assuming that blocking of a pore by a particle increases its resistance by twice the original resistance of the unblocked pore, we set $\rho_{\mathrm{b}} = 2$ for most simulations. The parameter $\eta = \Delta_{\mathrm{p}}/(4W^2 D)$ (see Table II) is initially set to 0.15, based on an assumption of approximately spherical large particles with radius of order W to calculate the effective particle volume Δ_{p}. Finally, the dimensionless cake permeability constant κ_{c} is set to 1. We demonstrate the effect of changing parameters λ_{c}, β_{m}, β_{c} and η, to model specific changes in caking conditions, as described below.

Before examining how depth-dependence in the initial membrane permeability [dictated by the choice of initial pore radius, $a(x, 0)$] affects results, we first investigate uniformly permeable membranes with initially cylindrical pores in order to focus on how caking affects filter performance. In Sec. V later we discuss how the initial pore shape may be chosen so as to improve performance.

For each simulation presented we solve the model numerically until the membrane becomes impermeable and the total flux through it falls to zero, at final time $t = t_{\mathrm{f}}$ (in all simulations this happens when the pore radius $a \to 0$ somewhere in the membrane). Our numerical scheme is straightforward, based on first-order accurate finite difference spatial discretization of the governing equations with a simple implicit time step in the pore-blocking Eq. (24), and trapezoidal quadrature to evaluate the necessary integrals.

Figure 2(a) shows the pore radius, $a(x, t)$, and concentrations of small particles within the membrane and the cake layer, $c_{\mathrm{m}}(x, t)$ and $c_{\mathrm{c}}(x, t)$, respectively, for a membrane with initially-cylindrical pores, at various times throughout the evolution, with parameter values as given in the figure caption. We note that in these simulations pore closure occurs first at the upstream membrane surface, consistent with the particle concentration graphs, which show that most of the deposition
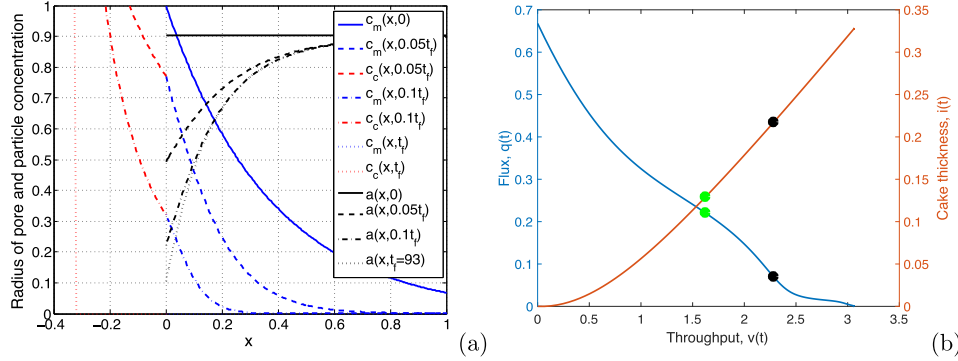
FIG. 2. Simulation for initially cylindrical pore $a(x, 0) = 0.904$ with $\lambda_m = 2$, $\lambda_c = 0.5$, $\beta_m = 0.1$, $\beta_c = 0.1$, $\rho_b = 2$, $\kappa_c = 1$, and $\eta = 0.15$. (a) Pore radius (black) and particle concentration (blue/red in membrane/cake) at several different times up to the final blocking time (t_f, indicated in the legend). (b) Instantaneous flux through membrane (blue) and cake thickness (red) vs. throughput. Green and black dots correspond to $t = 0.05t_f$ and $t = 0.1t_f$, respectively.

occurs at the pore inlet.[3] This effect becomes more pronounced at later times as the pore radius shrinks near the inlet, further enhancing the deposition there. The graphs of $c_m(x, t)$ and $c_c(x, t)$ demonstrate that for the chosen parameter set the filter membrane initially captures more than 90% of small particles (by adsorption), with this proportion increasing to nearly 100% at later times.

A common experimental characterization of membrane filtration performance is to plot a graph of the flux through the membrane at any given time, $q(t) = \int_0^1 u(x, t)dx$, versus the total volume of filtrate processed at that time [throughput $v(t)$, defined by $v(t) = \int_0^t q(t')dt'$]; the so-called flux–throughput graph for the membrane. We show this curve in Fig. 2(b), together with the dimensionless cake layer thickness versus throughput, with green and black dots corresponding to two selected times ($t = 0.05t_f$ and $t = 0.1t_f$, respectively) from the evolution shown in Fig. 2(a). The first observation from Fig. 2 is that, although in principle the filter remains operational until dimensionless time $t_f = 93$ (at which time the flux falls to zero), in practice by time $t = 0.05t_f$ the flux it sustains has already fallen to nearly 30% of its initial value, and by time $t = 0.1t_f$, flux is only about 10% of the initial value, making the filter extremely inefficient during the remaining 90–95% of its lifetime. Thus, even though the cake layer thickness is less than 15% of the membrane thickness at time $t = 0.05t_f$, its presence already has a significant adverse effect on the filtration efficiency, and the filter really should be discarded or cleaned by this time.

Furthermore, we see that the flux-throughput curve is initially concave in the early stages of filtration $t < 0.05t_f$, becoming convex for times $0.05t_f < t < 0.1t_f$. This change in curvature was observed in our previous work that accounted for adsorption and blocking [10], and also by other authors (including experimentally), e.g., Giglia and Straeffer [33]. Here, however, we now see that in the later stages of filtration ($t > 0.1t_f$), where the cake layer plays a dominant role, there is a second change of curvature of the flux-throughput curve to concave again, seen in Fig. 2(b) as the flux falls to zero (as discussed also by Griffiths *et al.* [9]). Again we emphasize that, although this regime of the filtration occupies 90% of the simulation time, the flux remains very low throughout, and only a modest additional throughput is achieved in this period.

―――――――

[3]This is not necessarily always the case; with appropriate choices of pore shape we are able to simulate filtration scenarios in which pore closure occurs at an internal point of the membrane. Such simulations, however, represent cases that are far from optimal, hence we do not present them here.

It is of particular interest to study the model parameters that principally govern the cake layer formation and its influence on membrane filter performance, since these have received little theoretical attention to date. Again, we do this first for the membrane with initially uniform permeability, in order to understand this case before considering depth-dependent permeability in Sec. V. Our model assumes that the cake is composed primarily of the large particles in the feed solution, thus the dimensional parameters Δ_p (the effective volume per large particle in the cake layer) and G (concentration of large particles in the feed) will be particularly important determinants of how fast the cake layer forms and grows. In order to study the effects of changing these parameters, we note that Δ_p appears in the definitions of β_c, λ_c, and η; while changes in G affect both β_m and β_c. We also study the effect of the cake fouling by varying the strength of attraction Λ_c between the small and large particles (via changes in β_c, λ_c), which governs adsorption within the cake layer.

Figure 3(a) illustrates the influence of changing the effective large-particle volume Δ_p occupied by the particles in the cake layer, for the uniform initial pore profile $a(x, 0) = 0.904$. As shown in Table II, variation of Δ_p affects three dimensionless parameters simultaneously: the dimensionless cake pore shrinkage rate, $\beta_c = 8\mu D \Lambda_c \Delta_p^{2/3} C_0/(\pi P_0 W^4 G)$; the dimensionless attraction coefficient between small and large particles, $\lambda_c = 32 \Lambda_c \mu D^2/(\pi P_0 W^2 \Delta_p^{1/3})$; and the dimensionless cake growth coefficient $\eta = \Delta_p/(4W^2 D)$ all change with Δ_p. Figure 3(a) shows results corresponding to four distinct values of Δ_p. Flux (blue curves) and cake thickness (red curves) are plotted against throughput for each of the four cases, which are distinguished by line styles. The results show a marked decrease in total throughput as Δ_p increases (increasing β_c, η; decreasing λ_c), in line with expectations: if the particles forming the cake layer are larger then the cake grows faster, meaning that system resistance increases sooner. The final cake layer thickness also increases with Δ_p, as one would anticipate. As with the previous figure, green and black markers are included to indicate when $t = 0.05t_f$ and $t = 0.1t_f$, respectively, in each simulation. We placed these markers on the cake thickness curves only, since these curves are well-separated; the corresponding marker on the companion flux curve would be vertically aligned with that on the cake thickness curve. Again these markers make clear that in many situations, the flux may drop to a low value quite early in the simulation, indicating that the filter may be very inefficient for much of the filtration. Perhaps surprisingly, this effect is less pronounced for the larger values of Δ_p, possibly because, although larger particles mean a thicker cake layer forms in the same time period (when compared to a cake composed of smaller particles), the thicker layer would also have a greater total void area. This could give rise to slower overall adsorptive blocking within the cake, with the performance-limiting adsorptive fouling actually occurring predominantly in the membrane.

To illustrate further the influence of the effective large-particle volume Δ_p, Fig. 3(b) shows throughput versus the dimensionless cake growth coefficient η, assumed to change due to variation of Δ_p (as in Fig. 3(a), β_c and λ_c are also assumed to change accordingly). Given the above observation about flux dropping rapidly relative to the total simulation time t_f, we plot three such throughput curves: total throughput $v(t_f)$ versus η; as well as $v(t_{10})$ and $v(t_{20})$ versus η, where t_{10}, t_{20} are defined by $q(t_j) = (j/100)q(0)$ (t_j is the time at which flux falls to $j\%$ of the initial value). The curves for $v(t_{10})$ and $v(t_{20})$ indicate that, particularly for larger values of η, there are not highly significant throughput gains to be made by continuing the filtration beyond time t_{20}. Moreover, for those physically relevant values of $\eta < 1$ where gains may appear reasonable, we see that the corresponding total filtration times t_f (plotted on the right-hand axis, red curve) are large, meaning that one would have to wait a long time to realize these potential additional gains in throughput.

As regards the trends with increasing η, note first that the total filtration time t_f decreases monotonically with η. This may be explained by the hypothesis advanced above: larger η means a thicker cake forms quickly, but with a large total void area. The performance-limiting adsorptive fouling then occurs within the membrane pores, meaning that pore closure actually occurs on timescales closer to those of the cake-free model. A cake layer composed of smaller particles gives rise to a thinner cake layer, but which fouls up more (spatially) uniformly. Flux then decreases
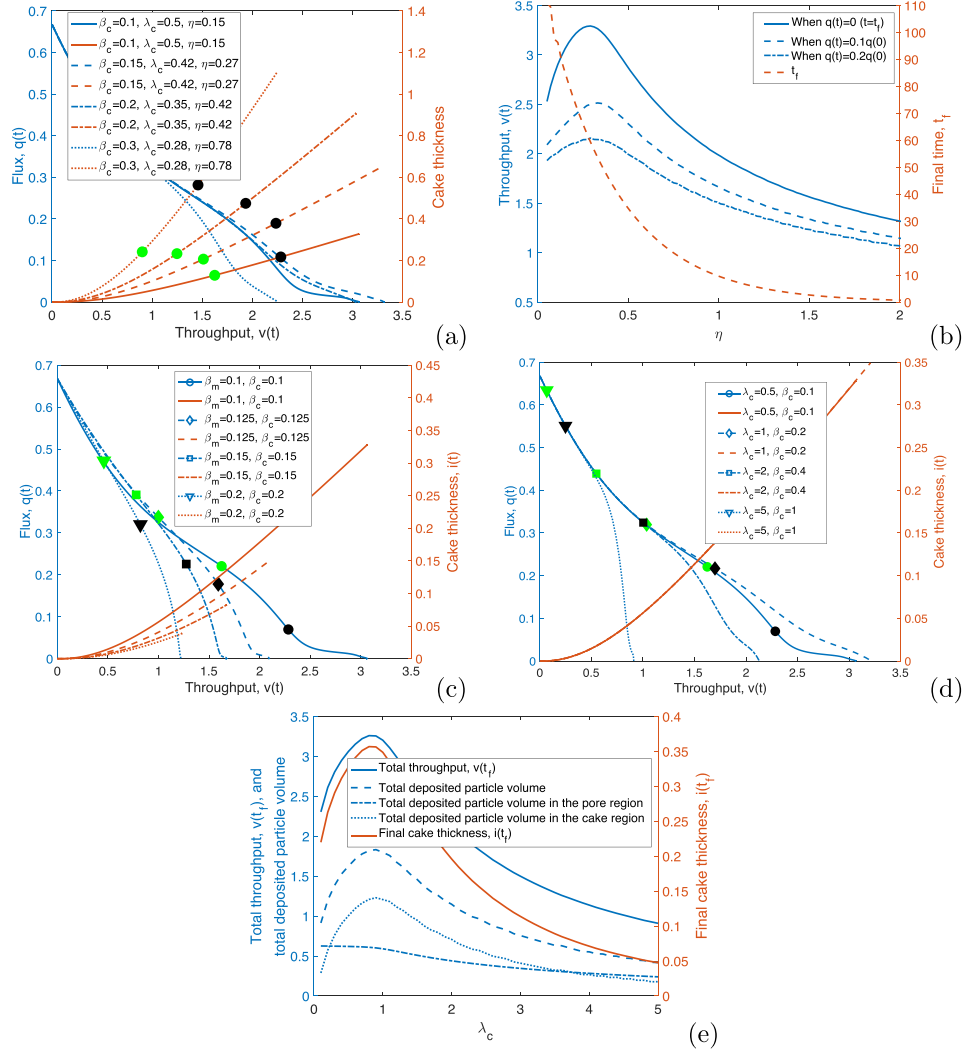
FIG. 3. Simulations for initially uniform pore $a(x, 0) = 0.904$, with $\lambda_m = 2$, $\rho_b = 2$, and $\kappa_c = 1$: (a) Flux (blue) and cake thickness (red) versus throughput with $\beta_m = 0.1$, for several values of Δ_p (effective large-particle volume), simulated by varying β_c, λ_c, and η [see Eqs. (30)–(32)]. (b) Throughput (blue) and t_f (red) versus η, corresponding to varying Δ_p as in (a). (c), (d) Flux (blue) and cake thickness (red) versus throughput with $\eta = 0.15$ as key caking parameters are varied: (c) varying G (large particle concentration) by varying β_m and β_c [see Eqs. (24) and (30)], with $\lambda_c = 0.5$; (d) varying Λ_c (attraction coefficient between large and small particles within cake) by varying λ_c and β_c [see Eqs. (30) and (31)], with $\beta_m = 0.1$. Green and black markers correspond to $t = 0.05t_f$ and $t = 0.1t_f$, respectively. (e) Total throughput $v(t_f)$, total deposited particle volume and final cake thickness $i(t_f)$ versus λ_c (varying Λ_c) with parameters as in (d).

to a trickle compared with the initial value, but due to the spatial uniformity of fouling the final pore closure takes a long time to achieve, giving a large t_f. Throughput initially increases as the effective large-particle volume Δ_p (or η) increases; but beyond some critical value of η ($\eta \approx 0.3$),

total throughput decreases rapidly. The validity of our model is likely restricted to the range $0.05 < \eta < 0.5$, over which variations in the outcome are not dramatic. It appears that a value around 0.3 could be desirable in terms of efficiency.

Figure 3(c) shows how varying the concentration of large particles in the feed, G, affects performance characteristics. Again, flux and cake layer thickness are plotted versus through-put for four distinct values of G. According to Table II, both the dimensionless cake pore shrinkage rate, $\beta_{\mathrm{c}} = 8\mu D\Lambda_{\mathrm{c}}\Delta_{\mathrm{p}}^{2/3}C_0/(\pi P_0 W^4 G)$, and the membrane pore shrinkage rate, $\beta_{\mathrm{m}} = 8\mu D\Lambda_{\mathrm{m}}\alpha C_0/(\pi P_0 W^5 G)$, change inversely proportionally to G, as also does our choice of timescale in Eq. (20), $T = 8\mu D/(\pi P_0 W^4 G)t$. We therefore change the values of β_{c} and β_{m} as well as rescaling time appropriately for each simulation. Our results demonstrate that, as G increases (β_{c} and β_{m} decrease), both the total throughput and the final cake thickness increase. With a higher concentration of large particles in the feed, the cake layer forms faster and acts as a secondary filter, which can also undergo adsorptive fouling. This continual creation of new "fresh" filter layer has the nonintuitive effect of prolonging the lifetime of the underlying filter membrane, resulting in a longer time to total blocking. The total throughput obtained over the entire duration of the filtration is increased, but takes much longer to achieve. As in Fig. 3(a) we again add green and black dots corresponding to $t = 0.05t_{\mathrm{f}}$, $t = 0.1t_{\mathrm{f}}$, respectively (though here we place them on the flux curves for greater ease of distinction).

In Fig. 3(d), the influence of the dimensional attraction coefficient between small and large particles in the cake, Λ_{c}, is illustrated for the uniform initial pore profile $a(x, 0) = 0.904$ (while other parameters are fixed as stated in the caption). According to Table II, the dimensionless cake pore shrinkage rate $\beta_{\mathrm{c}} = 8\mu D\Lambda_{\mathrm{c}}\Delta_{\mathrm{p}}^{2/3}C_0/(\pi P_0 W^4 G)$ and the dimensionless particle-particle attraction coefficient $\lambda_{\mathrm{c}} = 32\Lambda_{\mathrm{c}}\mu D^2/(\pi P_0 W^2 \Delta_{\mathrm{p}}^{1/3})$ both depend on Λ_{c}, therefore each must be changed proportional to Λ_{c} as it varies. Our results show that total filtrate throughput initially increases slightly with Λ_{c}, but ultimately decreases rapidly for larger values of Λ_{c}. The initial slight increase in filtrate throughput with Λ_{c} is somewhat puzzling, but the later decrease is as expected: larger values of Λ_{c} correspond to more rapid fouling of the forming cake layer, with attendant faster increase in system resistance. Possibly the initial increase in throughput with increasing Λ_{c} could be attributed to some tradeoff between faster fouling within the cake layer, but slower fouling in the membrane filter itself, with the net result that total system resistance in fact increases more slowly overall.

Figure 3(e) provides further context for this behavior. This figure shows the total throughput $v(t_{\mathrm{f}})$, the total deposited particle volume, and the final cake thickness $i(t_{\mathrm{f}})$ versus λ_c (corresponding to varying Λ_c) with the same parameters as in Fig. 3(d). The total deposited particle volume consists of two parts: the combined small and large particle volume accumulated within the cake layer; and the small particles that have deposited in the pore's interior (see blue dotted and dashed-dotted curves in Fig. 3(e), respectively). These are defined as $\int_{-I(T_{\mathrm{f}})}^{0}(2W)^2[1 - \phi_c(X', T_{\mathrm{f}})]dX'$ and $\int_{0}^{D} \pi[A^2(X', 0) - A^2(X', T_{\mathrm{f}})]dX'$, respectively (with the obvious dimensionless analogs), where T_{f} is the dimensional final time. These definitions assume that the deposited particles in the pore are tightly packed with no void area between them, while in the cake we simply use one minus its local porosity [see Eqs. (15) and (16)] to calculate the total particle volume. Again we see that the total throughput and the final cake thickness both initially increase with Λ_{c}, but the trend reverses around $\lambda_c = 1$. In addition, the total deposited particle volume in the cake follows the same behavior, while as λ_c increases, the total particle volume deposited in the pore decreases (as does the final filtration time t_{f}, not shown here). These results collectively illustrate the tradeoff between slower fouling in the membrane filter and faster fouling within the cake layer.

V. OPTIMIZING FOR THE MEMBRANE PORE PROFILE

A question of interest to manufacturers is: What is the optimum permeability profile as a function of depth through the membrane? For our model this question translates to: What is the optimal

shape of the filter pores? To answer this, we must first choose a measure of filtration performance. The most appropriate measure will vary depending on the user requirements, but for purposes of illustration, we consider the common experimental characterization of performance as the volume of filtrate collected over the filter lifetime (the throughput). We consider two possible definitions of filter lifetime: t_f, the time at which the membrane is completely blocked and flux $q(t)$ falls to zero; and t_{20}, the time at which flux falls to 20% of the initial value. Hence, our performance measures are $v(t_f) = \int_0^{t_f} q(t')dt'$, and $v(t_{20}) = \int_0^{t_{20}} q(t')dt'$, with larger values of either indicating superior performance.

The general optimization problem is very challenging, requiring consideration of pores of all possible shapes, so we simplify by restricting attention to the class of membranes with pores whose initial radius $a(x, 0)$ is polynomial in the depth of the membrane x,

$$a(x, 0) = a_0(x) = \sum_{i=0}^{n} b_i x^i. \tag{44}$$

To make a meaningful comparison, we compare performance of membranes that are similar in some quantifiable way. In our earlier work [10], we compared membranes with linear pore profiles and with the same initial net resistance to flow, $r(0)$, defined as

$$r(0) = \int_0^1 a^{-4}(x, 0)dx. \tag{45}$$

While tractable for the small class of linear pores, this approach becomes costly to implement for the wider class of polynomial pore profiles. However, for quite a range of different pore shapes and sizes, we have observed that membranes of the same initial net porosity, defined as

$$\bar{\phi}_m(0) = \frac{\pi}{4} \int_0^1 a^2(x, 0)dx, \tag{46}$$

(the factor of 1/4 because, with our nondimensionalization, each pore is confined within a box of area 4 units) have very nearly the same initial net resistance. [This appears to be true to within about 10% for porosities $\bar{\phi}_m(0) \in (0.6, \pi/4)$, where $\pi/4$ represents the maximum possible permeability for a circularly cylindrical pore enclosed in a box of square cross-section and touching the walls at four points.] We therefore compare filter membranes with the same net initial void fraction or porosity $\bar{\phi}_m(0) = \bar{\phi}_{m0}$. As we shall see, this is an easier problem.

We write the initial pore profile, which we suppose to be a polynomial of degree n, in terms of an orthogonal basis. Let $\tilde{P}_n(x)$ be the nth Legendre polynomial, an nth degree polynomial defined on $[-1, 1]$ that can be expressed via Rodrigues' formula [36],

$$\tilde{P}_n(x) = \frac{1}{2^n n!} \frac{d^n}{dx^n} [(x^2 - 1)^n]. \tag{47}$$

The $\tilde{P}_n(x)$ also satisfy the recursive formula

$$(n + 1)\tilde{P}_{n+1}(x) = (2n + 1)x\tilde{P}_n(x) - n\tilde{P}_{n-1}(x), \quad \text{where} \quad \tilde{P}_0(x) = 1, \quad \tilde{P}_1(x) = x. \tag{48}$$

An important property of the Legendre polynomials is that they are orthogonal with respect to the L^2 inner product on the interval $[-1, 1]$,

$$\int_{-1}^{1} \tilde{P}_n(x)\tilde{P}_m(x)dx = \frac{2}{2n + 1}\delta_{mn}. \tag{49}$$

This property underlies the advantage of using porosity rather than resistance in order to tackle the problem. The initial pore profile, $a_0(x)$ is defined on the interval [0,1], so we use an affine transformation to introduce the shifted Legendre polynomials as $P_n(x) = \tilde{P}_n(2x - 1)$, which can be calculated either from Eqs. (47) or (48). These shifted Legendre polynomials are also orthogonal,
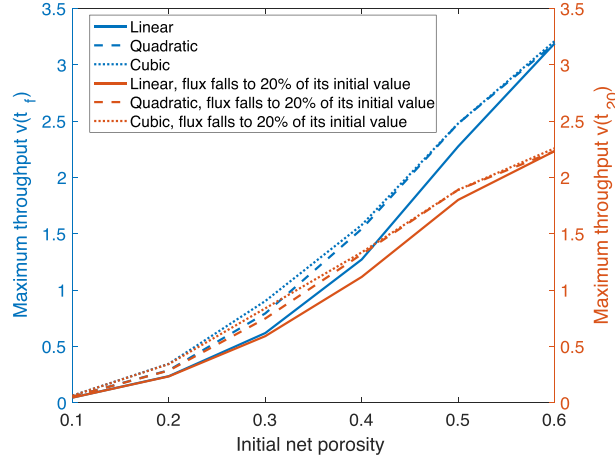
FIG. 4. Maximum throughput (at times t_f and t_{20}) versus initial net porosity $\bar{\phi}_{m0}$ [defined in Eqs. (46) or (52)] for the optimum linear, quadratic, and cubic initial pore profiles, with $\lambda_m = 2$, $\lambda_c = 0.5$, $\beta_m = 0.1$, $\beta_c = 0.1$, $\rho_b = 2$, $\kappa_c = 1$, and $\eta = 0.15$.

with

$$\langle P_i(x), P_j(x)\rangle_{L^2} = \int_0^1 P_i(x)P_j(x)dx = \frac{1}{2i+1}\delta_{ij} \tag{50}$$

[this follows trivially from Eq. (49)]. Next we write the initial pore profiles as

$$a_0(x) = \sum_{i=0}^{n} b_i P_i(x), \quad \text{where} \quad b_i = (2i+1)\int_0^1 a_0(x)P_i(x)dx, \tag{51}$$

where $P_i(x)$ is the ith degree shifted Legendre polynomial. Combining Eqs. (46) and (50) gives us the initial void fraction or porosity $\bar{\phi}_{m0} = \bar{\phi}_m(0)$ as

$$\bar{\phi}_{m0} = \frac{\pi}{4}\sum_{i=0}^{n}\frac{b_i^2}{2i+1}. \tag{52}$$

These results can be used to optimize for pore profiles in the class of polynomials as follows: for a chosen polynomial degree n and fixed value of the initial membrane porosity $\bar{\phi}_{m0}$, we sweep through the space of real coefficients b_i for $i \geqslant 1$ in small increments. For each set $\{b_i\}_{i=1}^n$ the lead coefficient b_0 can be determined from the fixed initial porosity via Eq. (52). Then, the filtration model is solved as discussed at the beginning of Sec. IV and we compute the flow, fouling and the total throughput for each polynomial profile. The optimum is the one that gives the maximum total throughput from the complete set considered (polynomials of fixed degree and equal net porosity). This process ensures that an optimum profile is always found.

A. Pore profile optimization study

In this subsection we briefly illustrate the implementation of the approach outlined above. Figure 4 shows the results of the optimization, plotting maximum throughput [$v(t_f)$ or $v(t_{20})$] obtained over all pores from the specified class, versus initial net membrane porosity $\bar{\phi}_{m0} = \pi/4 \int_0^1 a(x, 0)^2 dx$. We present results only for low-order polynomials (linear, quadratic, and cubic): our results indicate that in the intermediate porosity range, increasing the order of the polynomial describing the pore shape from 1 (linear) to 2 (quadratic) can lead to a reasonable increase (over
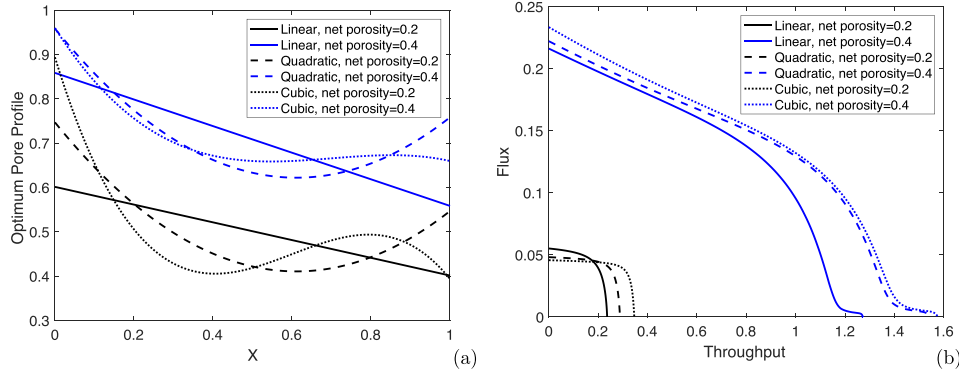
FIG. 5. (a) Optimum pore profiles; and (b) flux versus throughput for optimum profiles, optimized over the classes of linear, quadratic and cubic pore profiles. Results are shown for initial net membrane porosities $\bar{\phi}_{m0} = 0.2$ and 0.4 [defined in Eq. (46)], with $\lambda_m = 2$, $\lambda_c = 0.5$, $\beta_m = 0.1$, $\beta_c = 0.1$, $\rho_b = 2$, $\kappa_c = 1$, and $\eta = 0.15$.

10%) in total throughput; but that further increases in order lead to only negligible improvements, hinting (as expected) at convergence of performance to some global optimum as the degree of the approximating polynomial is increased.[4] As long as the membrane contains material to which particles can adhere—always guaranteed with our model assumptions of pores with circular cross-section, which ensures $0 < \bar{\phi}_{m0} \leqslant \pi/4$—pore closure within finite time is guaranteed in all cases, and thus a global optimum has to exist. We observe, furthermore, that when initial net porosity is small (close to zero) or large (close to $\pi/4$) the performance is almost independent of the polynomial degree.

The shapes of the optimum initial pore profiles computed, and their corresponding flux-throughput graphs, are shown in Figs. 5(a) and 5(b), respectively, for selected initial net porosities $\bar{\phi}_{m0} = 0.2$ and $\bar{\phi}_{m0} = 0.4$ (these values of ϕ_{m0}, which are small compared with those for typical membrane filters, were chosen for illustration only, in order to distinguish the graphs with relative ease: As the net porosity approaches the minimum and maximum values, zero and $\pi/4$, respectively, the optimum results necessarily converge to those for uniform cylindrical pores of zero and unit radius, respectively). We find that the optimal pore shapes are the same (or at least, indistinguishable) regardless of whether we maximize $v(t_f)$ or $v(t_{20})$. Consistent with the observations of Fig. 2(f), the optimal profiles in all six cases are widest at the upstream membrane surface, and the overall optima found in both cases $\bar{\phi}_{m0} = 0.2$ and $\bar{\phi}_{m0} = 0.4$ (the cubic profiles) are wider than both quadratic and linear pore profiles at the upstream side. The flux-throughput graphs [Fig. 5(b)] bear out the observation made in Sec. V: that membranes with the same net porosity have similar net resistance. This may be seen from the fact that the initial fluxes for pores with the same net porosity are very similar (surprisingly so for the low porosity case $\bar{\phi}_{m0} = 0.2$).

As already observed, and implied by Fig. 4, as the initial dimensionless net porosity increases towards the hypothetical maximum value $\pi/4$ (pore of unit radius contained in a square period-box of side length 2), the shape of the optimal initial pore profile converges to the linear case. Since most membranes in widespread use are rather permeable, these results suggest that (within the limitations of our modeling assumptions), optimizing only within the restricted class of linear pore profiles should provide a reasonable guide to the optimum permeability profile: Consideration of a larger class of pore profiles yields only small improvements.

---

[4]Note that total throughput can only increase as the degree of the polynomial is increased, because a polynomial of degree n is a special case of a polynomial of degree $n + 1$.
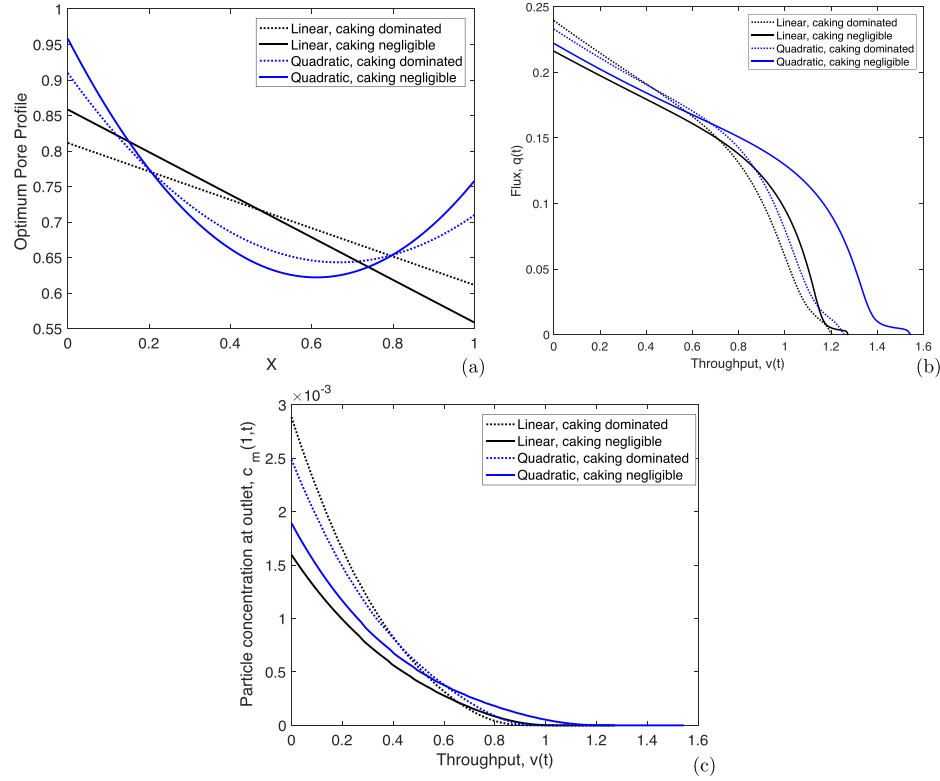
FIG. 6. (a) Optimum pore profiles based on maximizing $v(t_f)$, (b) corresponding flux-throughput graphs, and (c) particle concentration at the membrane outlet $c_m(1, t)$, versus throughput over the classes of linear and quadratic initial pore profiles respectively, with initial net membrane porosities $\bar{\phi}_{m0} = 0.4$, for caking dominated and negligible scenarios [corresponding to the dotted and solid curves in Fig. 3(a), respectively].

Finally, Fig. 6 shows optimized results [based on maximizing the total throughput, $v(t_f)$] for linear and quadratic pores with initial net membrane porosity $\bar{\phi}_{m0} = 0.4$. Two cases are distinguished here; (i) where the cake layer thickness and the membrane depth are comparable, which we call *caking dominated* and (ii) where the cake layer thickness is much less than the membrane thickness, termed *caking negligible*. These two scenarios correspond to different values of the effective volume per large particle in the cake layer Δ_p [see Fig. 3(a), where the dotted curves represent the identified caking-dominated scenario, while the solid curves represent negligible caking].

Our results [see Figs. 6(a) and 6(b)] show that there is a clear difference in the optimum pore profile in these two cases, with a larger pore profile gradient (higher permeability gradient in the depth of the membrane) proving advantageous when caking is negligible, while more uniform membrane permeability is desirable in a caking-dominated scenario. If one instead optimizes by maximizing $v(t_{20})$, then the results for the pore profile do not change appreciably in either regime.

Figure 6(c) shows the corresponding results for particle concentration in the filtrate, $c_m(1, t)$, for these optimum profiles, another key performance criterion. We observe that for these simulations, separation efficiency is higher when caking is negligible [$c_m(1, t)$ is less for this case than for the caking dominated scenario]. This provides further evidence to the conclusions drawn already, that significant caking is undesirable and should be avoided where possible. We note that a more

sophisticated optimization procedure would include some acceptable particle removal threshold in addition to maximizing filtrate throughput. This optimization would be more time-consuming, but not difficult, to carry out. In general, a high particle removal requirement conflicts with a high-throughput requirement, and the optimum membrane structure with a particle removal constraint added would represent the best tradeoff between maximizing throughput while obtaining a sufficiently clean filtrate.

VI. CONCLUSIONS

We have proposed a model for the formation and growth of a cake layer on the upstream side of a planar membrane filter in dead-end filtration. This fouling cake layer may form simultaneously with other fouling modes: pore blocking (sieving) by large particles, which acts to increase the resistance of the blocked pore; and adsorption of small particles within pores, which increases pore resistance by shrinking the pore diameter (see Ref. [10]). It is the large pore-blocking particles that are assumed to form the growing cake layer, with the smaller particles that lead to adsorptive fouling settling in the cake interstices, as well as in the membrane pores. A key motivation for our work is to derive a model capable of describing a wide range of different filtration scenarios. As such, though our model can simulate scenarios in which all fouling mechanisms are operating simultaneously, it can also just as easily describe situations where there is only one fouling mechanism, or any 2 of the 3 included. In this context we note the results of Duclos-Orsello *et al.* [30], who find that even for datasets where a single filtration mode is dominant, three fouling mechanisms are in fact in operation, and a good model is capable of distinguishing, from flux-throughput data, which modes are operational at which stages of filtration.

Since the model incorporates three distinct fouling modes it necessarily contains a number of parameters. To keep the investigation manageable, the effects of just a few, most relevant to the caking, are investigated: Δ_p, the effective large-particle volume; G, the concentration of large particles in the feed; and Λ_c, the dimensional attraction coefficient between large and small particles within the cake (which governs how fast the permeability of the caking layer changes). The effects of varying these parameters are probed by varying the associated dimensionless parameters. Other model parameters are held fixed in our investigations, with (we believe plausible) values, summarized in Tables I and II. Thus, our results as presented are intended to be illustrative of our model's capability to provide useful information, given reliable parameter estimates; they are not necessarily representative of any particular experiment.

Our model allows us to simulate a filtration until the time at which pores are completely blocked and the flux through the membrane falls to zero. Though in principle this blockage could occur anywhere within the membrane-cake structure, our results indicate that pore closure typically occurs first at the upstream membrane surface, which means that the adsorptive fouling is greatest at the membrane pore inlet. This effect becomes self-reinforcing at later times as the pore radius shrinks near the inlet, further enhancing the deposition there. We could, by suitable choice of parameters, present simulations in which pore closure occurs at an internal point, but such simulations would in general be nonoptimal, with poor filter lifetime.

We also observe that cake formation actually prolongs the lifetime of a filter, in the sense that the time to total blocking is longer relative to the model with no caking. However, the price for this extended lifetime is extreme inefficiency: the flux through the filter drops quickly and filtration is very slow, even for scenarios where the cake layer thickness is much less than the membrane thickness. Our results also show that as we increase either of the key parameters Δ_p and G, the cake layer growth-rate increases, as does its final thickness. In the former scenario, a critical value of Δ_p is identified, which yields a maximal total filtrate throughput over the filter lifetime [see Fig. 3(b)], while in the latter case the total throughput always decreases as G increases.

Finally, we illustrate how membrane pore structure can be optimized with respect to simple performance criteria, for a range of initial net membrane porosities and operating conditions. Considering the initial pore profile to be a polynomial function in the depth of the membrane

x, it is found that low-order polynomials are sufficient to give a membrane with near-optimal performance; and that for high-porosity membranes of the type often used in applications, a linear pore profile should suffice. Our results also show that for scenarios in which the cake layer thickness remains small compared to the membrane thickness (caking negligible), the optimal membrane has a higher permeability gradient (with pores larger on the membrane's upstream side), relative to that for a scenario where caking dominates (with cake layer thickness comparable to the membrane thickness).

---

[1] E. Iritani, A review on modeling of pore-blocking behaviors of membranes during pressurized membrane filtration, Drying Tech. **31.2**, 146 (2013).

[2] G. Bolton, D. LaCasse, and R. Kuriyel, Combined models of membrane fouling: Development and application to microfiltration and ultrafiltration of biological fluids, J. Membrane Sci. **277**, 75 (2006).

[3] G. R. Bolton, A. W. Boesch, and M. J. Lazzara, The effect of flow rate on membrane capacity: Development and application of adsorptive membrane fouling models, J. Membrane Sci. **279**, 625 (2006).

[4] C.-C. Ho and A. L. Zydney, Effect of membrane morphology on the initial rate of protein fouling during microfiltration, J. Membrane Sci. **155**, 261 (1999).

[5] C.-C. Ho and A. L. Zydney, A combined pore blockage and cake filtration model for protein fouling during microfiltration, J. Colloid Interface Sci. **232**, 389 (2000).

[6] H. K. Lonsdale, The growth of membrane technology, J. Membrane Sci. **10**, 81 (1982).

[7] L. Fillaudeau and H. Carrere, Yeast cells, beer composition and mean pore diameter impacts on fouling and retention during cross-flow filtration of beer with ceramic membranes, J. Membrane Sci. **196**, 39 (2002).

[8] R. G. M. Van der Sman, H. M. Vollebregt, A. Mepschen, and T. R. Noordman, Review of hypotheses for fouling during beer clarification using membranes, J. Membrane Sci. **396**, 22 (2012).

[9] I. M. Griffiths, A. Kumar, and P. S. Stewart, A combined network model for membrane fouling, J. Coll. Int. Sci. **432**, 10 (2014).

[10] P. Sanaei and L. J. Cummings, Flow and fouling in membrane filters: Effects of membrane morphology, J. Fluid Mech. **818**, 744 (2017).

[11] P. Sanaei and L. J. Cummings, Membrane filtration with complex branching pore morphology, J. Phys. Rev. Fluids **3**, 094305 (2018).

[12] https://www.math2market.com/

[13] M. Rahimi, S. S. Madaeni, M. Abolhasani, and A. A. Alsairafi, CFD and experimental studies of fouling of a microfiltration membrane, Chem. Eng. Process.: Process Intens. **48**, 1405 (2009).

[14] R. Ghidossi, D. Veyret, and P. Moulin, Computational fluid dynamics applied to membranes: State of the art and opportunities, Chem. Eng. Process. **45**, 437 (2009).

[15] G. A. Fimbres-Weihs and D. E. Wiley, Review of 3D CFD modeling of flow and mass transfer in narrow spacer-filled channels in membrane modules, Chem. Eng. Process.: Process Intens. **49**, 759 (2010).

[16] G. Keir and V. Jegatheesan, A review of computational fluid dynamics applications in pressure-driven membrane filtration, Rev. Environ. Sci. Bio/Technol. **13**, 183 (2014).

[17] W. Naessens, T. Maere, N. Ratkovich, S. Vedantam, and I. Nopens, Critical review of membrane bioreactor models, Part 2: Hydrodynamic and integrated models, Bioresour. Technol. **122**, 107 (2012).

[18] E. Iritani and N. Katagiri, Developments of blocking filtration model in membrane filtration, KONA Powder Part. J. **33**, 179 (2016).

[19] I. L. Chernyavsky, L. Leach, I. L. Dryden, and O. E. Jensen, Transport in the placenta: Homogenizing haemodynamics in a disordered medium, Philos. Trans. R. Soc. A **369**, 4162 (2011).

[20] K. R. Daly and T. Roose, Homogenization of two fluid flow in porous media, Proc. R. Soc. A **471**, 20140564 (2015).

[21] M. P. Dalwadi, I. M. Griffiths, and M. Bruna, Understanding how porosity gradients can make a better filter using homogenization theory, Proc. R. Soc. A **471**, 2182 (2015).

[22] I. M. Griffiths, A. Kumar, and P. S. Stewart, Designing asymmetric multilayered membrane filters with improved performance, J. Membrane Sci. **511**, 108 (2016).

[23] J. B. Keller, Darcy's law for flow in porous media and the two-space method (Stanford Univ., CA, 1980), https://apps.dtic.mil/dtic/tr/fulltext/u2/a095629.pdf.

[24] R. Penta, D. Ambrosi, and R. J. Shipley, Effective governing equations for poroelastic growing media, Q. J. Mech. Appl. Math. **67**, 69 (2014).

[25] R. Penta, D. Ambrosi, and A. Quarteroni, Multiscale homogenization for fluid and drug transport in vascularized malignant tissues, Math. Models Methods Appl. Sci. **25**, 79 (2015).

[26] G. Richardson and S. J. Chapman, Derivation of the bidomain equations for a beating heart with a general microstructure, SIAM J. Appl. Math. **71**, 657 (2011).

[27] X. R. Fernández, I. Rosenthal, H. Anlauf, and H. Nirschl, Experimental and analytical modeling of the filtration mechanisms of a paper stack candle filter, Chem. Eng. Res. Des. **89**, 2776 (2011).

[28] W. W. Li, G. P. Sheng, Y. K. Wang, X. W. Liu, J. Xu, and H. Q. Yu, Filtration behaviors and biocake formation mechanism of mesh filters used in membrane bioreactors, Sep. Purif. Technol. **81**, 472 (2011).

[29] K. Nakamura, T. Orime, and K. Matsumoto, Response of zeta potential to cake formation and pore blocking during the microfiltration of latex particles, J. Membrane Sci. **401**, 274 (2012).

[30] C. Duclos-Orsello, W. Li, and C. C. Ho, A three mechanism model to describe fouling of microfiltration membranes, J. Membrane Sci. **280**, 856 (2006).

[31] P. Sanaei, G. W. Richardson, T. Witelski, and L. J. Cummings, Flow and fouling in a pleated membrane filter, J. Fluid Mech. **795**, 36 (2016).

[32] R. Probstein, *Physicochemical Hydrodynamics, An Introduction*, 2nd ed. (Wiley Interscience, Hoboken, NJ, 1994).

[33] S. Giglia and G. Straeffer, Combined mechanism fouling model and method for optimization of series microfiltration performance, J. Membrane Sci. **417**, 144 (2012).

[34] A. Kumar, private communication (2014).

[35] N. B. Jackson, M. Bakhshayeshi, A. L. Zydney, A. Mehta, R. van Reis, and R. Kuriyel, Internal virus polarization model for virus retention by the Ultipor VF grade DV20 membrane, Biotechnol. Prog. **30.4**, 856 (2014).

[36] M. Abramowitz and I. A. Stegun, *Handbook of Mathematical Functions: With Formulas, Graphs, and Mathematical Tables* (Courier Corporation, North Chelmsford, MA, 1964), Vol. 55.